Characterization of nano-crystalline ZrO_2 synthesized via reactive plasma processing

S. Jayakumar [a,*], P.V. Ananthapadmanabhan [b], , K. Perumal [c], T.K. Thiyagarajan [b], S.C. Mishra [d], L.T. Su [e], A.I.Y. Tok [e] and J Guo[e]

[a]Research and Development Centre, Bharathiar University, Coimbatore – 64 1014, India. [b] Laser and Plasma Technology Division, BARC, Trombay, Mumbai – 400 085, India. [c]Department of Physics, Sri Ramakrishna Mission Vidyalaya College of Arts & Science, Coimbatore – 641 020. [d]Department of Metallurgical & Materials Engg, National Institute of Technology, Rourkela – 769 008, India. [e]School of Materials Science & Engg, Nanyang Technological University, 50 Nanyang Avenue, Singapore – 639 798. sjayakumar.physics@gmail.com

Abstract:

Nano-crystalline ZrO_2 powder has been synthesized via reactive plasma processing. The synthesized ZrO_2 powders were characterized by X-ray diffraction (XRD), Raman spectroscopy, transmission electron microscopy (TEM) and FTIR spectroscopy. The synthesized powder consists of a mixture of tetragonal and monoclinic phases of zirconia. Average crystallite size calculated from the XRD pattern shows that particles with crystallite size 20nm or less than 20 nm are in tetragonal phase, whereas particles greater than 20nm are in the monoclinic phase. TEM results show that particles have spherical morphology with maximum percentage of particles distributed in a narrow size from about 15 nm to 30 nm.

Keywords: Nano-crystalline material, Reactive plasma processing, Zirconium oxide

1. Introduction

Zirconium oxide is a refractory material having high strength, high fracture toughness, excellent chemical resistance and low thermal conductivity. These properties of ZrO_2 make it highly useful in the field of structural, mechanical and high temperature applications [1-2]. Pure zirconia exists in three crystallographic modifications-namely, monoclinic, tetragonal and cubic phases [3-5]. Monoclinic form of zirconia is the thermodynamically stable phase at room temperature, whereas tetragonal and cubic are stable at high temperatures. Monoclinic zirconia transforms reversibly to the tetragonal phase when heated to about 1170°C and as the temperature exceeds 2370°C, the tetragonal phase transforms into the cubic phase.

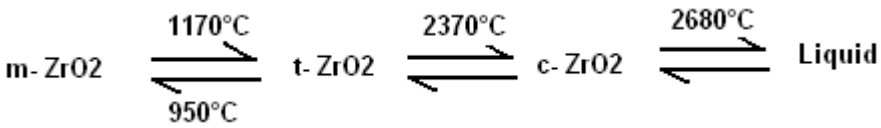

However, the high temperature phases may be stabilized at room temperature either by adding suitable dopants or by reducing the particle size into the nanometer regime [6]. The stabilization by the latter way (nano particles) has attracted considerable interest because of the large surface area, unusual adsorptive properties, surface defects, fast diffusivities and superplasticity of the nano-sized powder [7-8]. It is reported that nano-crystalline ZrO_2 is used as an effective catalyst for isosynthesis and catalyst carrier for Fe_2O_3 for selective catalytic reduction (SCR) of NO_x due to its high thermal stability and unique bifunctional character of weak acidic and base properties [9-11]. ZrO_2 is of great technological and scientific interest because of its potential applications in oxygen sensors, solid electrolytes, electrodes and fuel cells due to oxygen ion conductivity and rich oxygen defects in surface [12-16]. Besides, it is also used as a photocatalyst to degrade organic pollutants and dyes like rohdamine B (RhB) [17, 18].

A key requirement for most of the above mentioned applications is to obtain nano-crystalline ZrO_2 with high specific surface area and enhanced crystallinity [9-18]. This has been achieved by several synthesis methods, which include hydrothermal, solgel, co-precipitation, and flame synthesis [19-22]. Electric arc discharge, microwave irradiation, pechini type sol-gel process and sonochemical method are also reported recently to synthesize nano ZrO_2 [23-26].

The present paper reports synthesis of nano-crystalline ZrO_2 by reactive plasma processing (RPP) and its characterization. Reactive plasma processing (RPP) is a novel technique, which takes the advantage of the high temperature and high enthalpy of the thermal plasma jet to effect 'in-flight' chemical reactions in the presence of reactive gas to synthesize nano-sized powders of advanced ceramics, novel coatings and convert minerals and industrial wastes to value added materials [27-29]. The technique can also be used to produce spherical powders of metals and ceramics for special applications [30]. The high quench rate, which is characteristic of the process, favours homogeneous nucleation resulting in nano-sized particles. The major advantages of the reactive plasma processing includes versatility, short processing time, large throughput, adaptability to process thin films and coatings.

The objective of the present work is to synthesize nano-crystalline ZrO_2 using ZrH_2 powder by reactive plasma processing. Phase composition, crystallite size and morphology of the synthesized samples are investigated. The novelty of this method lies in the fact that starting from micron-sized powder precursor, we have synthesized nanocrystalline zirconium oxide.

2. Experimental procedure

2.1 Reactive plasma synthesis of nano-crystalline ZrO2

A schematic block diagram of the experimental setup used for the synthesis of nano-crystalline ZrO2 is shown in Fig 1. The main component of the plasma reactor is a 40KW DC non-transferred arc plasma torch, which generates high temperature and high velocity plasma jet. The plasma torch consists of a water cooled copper anode and tungsten

cathode with water-cooled electrical power cables that are connected to a 40 kW DC power supply. It also has provision to feed plasma forming gas and precursor powder. The torch flange is mounted on a water-cooled stainless steel reactor. The powder is stored in a powder feeder and is injected into the plasma jet through a side port provided at the anode of the plasma torch. Oxygen or any desired reactive gas can be injected downstream the plasma jet, by means of a gas injector ring fitted on the torch head section. The product can be collected from various segments of the plasma reactor. There is a master control console, which controls and monitors all the process parameters such as arc voltage, arc current, gas flow, powder feed rate, water flow rate, etc.

A mixture of Ar and N_2 was used as the plasma gas. The DC arc was struck between the cathode and anode. Input power to the plasma torch was varied from 10-16 kW by controlling gas flow rate and arc current. The range of operating parameters is given in Table 1. The precursor material used was ZrH_2 powder with 99.8% purity from CERAC, USA. ZrH_2 powder (38-53μm size). The precursor powder was injected into the plasma jet by using argon as the carrier gas. Oxygen gas was introduced 10mm downstream of the exit of the plasma torch. ZrH_2 dissociates to form Zr particles and hydrogen gas in the plasma jet that are subsequently converted to ZrO_2 and water vapor, which escapes along with the exhaust gas stream. The nano-crystalline ZrO_2 formed settles on the walls of the reactor and collection chamber as fine powder. Powders collected from various regions of plasma reactor were identified as given in Table 2 and were characterized by X-ray diffraction, TEM, Raman and FTIR spectroscopy.

2.2 Powder characterization

The zirconia powder samples collected from different locations of the plasma reactor were characterized by x-ray powder diffraction, Raman and FTIR spectra analysis for their phase composition. X-ray diffraction (XRD) patterns of the synthesized samples were recorded on a Bruker D8 advanced X-ray powder diffractometer. Ni- filtered Cu k-α radiation in θ-2θ geometry was used for recording the diffraction patterns. Fourier transform Raman spectra were recorded on a Bruker RFS 100 system (Ettlingen, Germany) using the 1064 nm line emitted by a CW diode pumped Nd: YAG laser as the excitation source. Fourier transform infrared spectroscopy (Spectrum one: FTIR spectrometer, Perkin Elmer, 450-4000 cm^{-1}, KBr pellet technique) was used to identify the vibrational features of the samples. Particle size and morphology of the samples were carried out using JEOL transmission electron microscope (JEM 2100F, Japan) operated at 200 KV.

3. Results and discussion

3.1 X-ray diffraction and Phase structure

X-ray diffraction patterns of nano-crystalline ZrO_2 powder synthesized at different plasma power are shown in figure 2. The diffraction patterns show that the synthesized powder is a mixture of monoclinic and tetragonal phase corresponding to JCPDS files 37-1484 and 79-1771 respectively. However, diffraction peaks of zirconium metal (very low intensity) and unreacted ZrH_2 are also seen in the powder synthesized at 10 kW, indicating that the power was not sufficient to effect complete conversion of the ZrH_2 to ZrO_2. The powder samples synthesized at 12 kW and 16 kW, on the other hand, show only the monoclinic and tetragonal phases of zirconium oxide. This shows that the precursor powder (ZrH_2) is completely converted into zirconium oxide at 12 kW and 16 kW. The nano-crystalline zirconium dioxide powder sample synthesized at 16 kW has been used for all further analysis.

Figure 3 shows the diffraction patterns of samples (synthesized at 16 kW) collected from different locations of the plasma reactor. The samples are seen to consist of the monoclinic and tetragonal phase of ZrO_2, their relative amounts being different in the three samples. The relative amount of the tetragonal phase present in the samples was calculated from the following relation.

$$X_t = \frac{I_t(111)}{I_t(111) + I_m(111) + I_m(-111)} \times 100 \qquad (1a)$$

$$X_m = 100 - X_t \qquad (1b)$$

Where X_t and X_m stand for the weight percentage of the tetragonal and monoclinic phases respectively, whereas I_t and I_m are the intensities of their diffraction peaks.

It is evident from figure 3 that the phase structure of the different samples collected from torch head region (A), the reactor wall (B) and flanges of collection chamber(C) consist of a mixture of the monoclinic phase and the tetragonal phase. However, the relative amounts of the monoclinic and tetragonal phases were different in the samples as shown in Table 3. It is observed that sample collected from the flanges of the collection chamber has the highest amount of the tetragonal phase. The monoclinic form of ZrO_2 is the major phase in the sample collected from the torch head region (A).

The crystallite size was evaluated based on the Scherrer equation [31].

$$D_{hkl} = \frac{K\lambda}{B_{hkl}\ COS\theta} \qquad (2)$$

Where λ stands for the wavelength of the incident x-ray, B for full width at half maximum (after correcting for instrumental broadening), θ is the corresponding Bragg angle and K=0.94 for spherical particle. The average crystallite sizes of the monoclinic phase, calculated from the (-111) and (111) diffraction peaks were found to be 34 nm, 27 nm and 26 nm for the powder samples A, B and C. Similarly, the average crystallite

sizes, calculated from the (111) diffraction peak of the tetragonal phase, were found to be 17 nm, 19 nm and 20 nm for samples A, B and C respectively.

These results show that monoclinic phase of zirconia is stable when the crystallite sizes is above 20 nm, whereas the metastable tetragonal phase is stabilized below 20nm. These results agree reasonably well that reported by Garvie, who attributed the formation of metastable tetragonal phase to the critical crystallite size effect [6]. Garvie experimentally showed the existence of a critical size of ~ 30 nm, below which the metastable tetragonal phase is stablilized in zirconium oxide. The monoclinic phase is the stable phase when the crystallite size is above 30 nm.

3.2 FT Raman Spectroscopy

Results of Raman spectra of the samples corroborate the findings of XRD analysis. Figure 3 shows the Fourier Transformed Raman spectrum of the sample C. Seventeen bands are observed as shown in the figure. As predicted by factor group analysis, the monoclinic phase should have 18 (9Ag+9Bg) and tetragonal phase should have 6 (A1g+2B1g+3Eg) Raman active vibrational modes [32]. Among the 18 Raman active vibrational modes of monoclinic ZrO2, 15 are observed and they are assigned as follows: Bg at 86 cm^{-1}, Ag at 103 cm^{-1}, at 180 cm^{-1} and at 191 cm^{-1}, Bg at 223 cm^{-1}, Ag at 307 cm^{-1}, Bg at 335 cm^{-1}, Ag at 347 cm^{-1}, Bg at 382 cm^{-1}, Ag at 476 cm^{-1}, Bg at 502 cm^{-1} and at 538 cm^{-1}, Ag at 559 cm^{-1}, Bg at 616 cm^{-1} and Ag at 637 cm^{-1}. The observed values match very well with the reported Raman spectra for monoclinic zirconia [33-34]. Bands occurring at 147 cm^{-1} and 267 cm^{-1} are the characteristic Raman active modes of tetragonal ZrO2. Besides, bands observed at 476 cm^{-1} and 637 cm^{-1} are observed in both tetragonal and monoclinic phases of ZrO2. These observed bands corresponding to t-ZrO2 are assigned as follows: B1g at 147 cm^{-1}, Eg at 267 cm^{-1}, at 476 cm^{-1} and at 637 cm^{-1} [35-36]. Raman spectra of sample A and B are found to be y similar to that of sample C.

3.3 FT-IR analysis

Figure 4 shows the FT-IR spectrum of the sample C. Bands observed at 3428 cm^{-1} and 1634 cm^{-1} are assigned to the bending and stretching vibrations of the O-H bond due to absorbed water molecules. The band at 1384 cm^{-1} is attributed to the absorption of non-bridging OH groups. The sharp band at 746 cm^{-1} is the characteristic of m-ZrO_2. A broad band with a peak at 542cm^{-1} and a shoulder at 627cm^{-1} is ascribed to Zr-O vibrations of t-ZrO_2 [37]. However, weak peaks in the range 460 cm^{-1} to 690 cm^{-1} corresponding to m-ZrO_2 are not observed due to dilution effect (presence of tetragonal (44%) phase). A similar observation was reported by Chen at al [38] for pure zirconia nanoparticles.

3.4 TEM observations

Transmission electron microscope (TEM) photographs of reactive plasma synthesized nano ZrO_2 are shown in figure 6(a-c). The corresponding particle size distribution is shown in figure 6 (d-f) as bar charts alongside the TEM micrographs. Individual particles are well resolved and their spherical morphology is evident from the figures. It is seen from particle size distribution more than 90% of the particles are below 25 nm. However, a very small fraction of particles are found to have size below 4 nm and above 30 nm. It was observed that there was significant variation in size distribution of particles collected from different locations. It is seen from TEM results that powder collected from the torch head zone (A), has maximum number of coarser particles. On the other hand, the powder sample collected from the flanges on the collection chamber (C) has about 75% of the particles in the size below15 nm. It is also observed that the relative amount of the tetragonal phase increases with the amount of finer particles.

3.5 Discussion

The 'inflight' formation of nano-crystalline zirconia particles can be explained as follows: When zirconium hydride particles enter the plasma jet, they melt and the molten droplets react with oxygen gas injected downstream, leading to the formation of zirconium oxide. Due to the large amount of heat released during the formation of zirconium oxide and the high temperature of the plasma jet, zirconium oxide that is formed further melts and dissociates into ZrO(g), Zr vapor and oxygen. Zirconium vapor and ZrO(g) move downstream and react with oxygen to form molecular clusters of ZrO_2 that condense on the cold wall of the reactor as nano sized spherical particles. The high quench rate inhibits grain growth and favours the formation of nano-crystalline powder. Formation of nano-structurally stabilized metastable phases in reactive plasma processing has been reported by Ananthapadmanabhan et al [27, 39]. These authors have studied in detail the 'inflight' formation of nano-crystalline alumina and titania in a thermal plasma jet.

It is seen from table 3 that there is considerable variation in the phase composition of the powders collected from various locations of the plasma reactor. The tetragonal content in the product increases from sample A to C. This observed variation of phase composition in different regions can be explained as follows.

As the particles traverse the plasma jet, larger particles(>20 nm) tend to collect on the torch head and top of the reactor wall, whereas particles below 20 nm tend to float in the gas and settle on the lower side of the reactor wall and side flanges of the collection chamber. Further the gas temperature is higher near the torch head boundary and this "thermal effect" favors cluster growth and particle association leading to bigger particle

size on the torch head. Thus, the fraction of large-sized particles (>20 nm) is more in the powder sample collected from the torch head section compared to that collected from the flanges on the collection chamber. Since smaller particle size favors the formation of the tetragonal phase, powder sample collected from the flanges on the collection chamber (C) has a relatively larger concentration of the tetragonal phase. On the other hand, powder collected from the torch head has a higher percentage of larger particles and consequently higher concentration of the monoclinic phase.

Close scrutiny of the x-ray diffraction, Raman spectroscopy and TEM results of the samples collected from the different locations lead to interesting analysis. It is seen that as the particle size decreases, the relative amount of the tetragonal phase increases. It is also evident from the various results that the tetragonal phase gets stabilized as the particle size goes below about 20 nm. Particle size distribution in the samples collected from different locations shows that powder collected from the flanges in the collection chamber (i.e. the farthest end from the plasma torch), sample C, has the maximum amount of the finest fraction, whereas that collected from the torch head end has the maximum amount of coarser particles. Particle size distribution in sample B(ie. from the reactor wall) lies between those of A and C.

The synthesis of nanocrystalline powders of zirconia often produces the tetragonal phase, which for coarse-grained powders is stable only at high temperatures and transforms into the monoclinic form on cooling. However, as the particle size approaches nano-scale, surface energies become significant in stabilizing the tetragonal phase. This stability reversal has been suggested to arise due to differences in the surface energies of the monoclinic and tetragonal polymorphs. Monoclinic ZrO2 was found to have the largest surface enthalpy and amorphous zirconia the smallest [40]. Therefore, with increasing surface area (decreasing particle size), the monoclinic phase becomes less stable and the tetragonal phase gets stabilized. Garvie had proposed a critical size of ~ 30 nm, below which the metastable tetragonal phase is stablilized in zirconium oxide [6]. However, Michael W. Pitcher et al have recently shown that apart from crystallite size, there are other factors such as presence of water molecules, lattice strain, impurities, etc that can influence phase structure [40-43]. This possibly explains the reason for the observation of monoclinic phase even below 30nm in the present study.

Conclusion

A one-step process to synthesize nanocrystalline ZrO_2 powder by reactive plasma processing is reported in this work. Zirconium hydride was used as precursor material, which was injected into the plasma jet and allowed to react with oxygen to form nano-sized ZrO_2 powder. X-ray diffraction results show that the product is a mixture of monoclinic and tetragonal phase with larger sized particles (>20nm) having the monoclinic structure and the finer particles ($\leq$ 20) having the tetragonal structure. FT-Raman, FTIR and TEM studies confirm the results of XRD.

References

[1]B. Basu, Int. Mater. Rev. 50 (2005) 239–256.

[2]I.Berkby, R. Steven, Key. Eng. Mater. 122-124 (1996) 527.

[3]Kisi EH, Howard CJ, Key. Eng. Mater 153–154 (1998) 1–36.

[4]Shukla S, Seal S, Int. Mater.Rev. 2005, 50, 45.

[5]Bohe A.E, Andrade-Gamboa J, Pasquevich D.M, Tolley A, Pelegrina J.L, J.Am. Ceram. Soc. 83(4) (2000) 755

[6]Garvie R.C., J. Phys. Chem. 69 (1965), 1238.

[7]H.D. Gesser, P.C. Goswami, Chem. Rev. 89 (1989) 765.

[8]C. Suryanarayana, C.C. Koch, Hyperfine Interactions 130 (2000) 5-44

[9]Watcharapong Khaodee, Bunjerd Jongsomjit, Piyasan Praserthdam, Shigeo Goto, Suttichai Assabumrungrat, J. Mol. Catal. A: Chem. 280 (2008) 35–42

[10]N. Apostolescu, B. Geiger, K. Hizbullah, M.T. Jan, S. Kureti, D. Reichert, F. Schott, W. Weisweiler, Appl. Catal. B 62 (2006) 104–114

[11]S. Djerad, B. Geiger, F.J.P. Schott, S. Kureti, Catalysis Communications 10 (2009) 1103–1106

[12]M. Maczka, E.T.G. Lutz, H.J. Verbeek, K. Oskam, A. Meijerink, J. Hanuza, M. Stuivinga, J. Phys. Chem. Solids 60 (1999) 1909–1914

[13]Andreas Ziehfreund, Ulrich Simon, Wilhelm F. Maier, Adv. Mater. 8 (1996) 424-427

[14]F.P.F. van Berkel, F.H. van Heuveln, J.P.P. Huijsmans, Solid State lonics 72 (1994) 240-247

[15]Henk Verweij, Adv. Mater. 10 (1998) 1483-1486

[16]Marc Mamak, Neil Coombs, Geoffrey Ozin, J. Am. Chem. Soc, 122 (2000) 8932-8939

[17]He Zheng, Kaiyu Liu, Huaqiang Cao, Xinrong Zhang, J. Phys. Chem. C 113 (2009) 18259–18263

[18]Guohui Tian, Kai Pan, Honggang Fu, Liqiang Jing, Wei Zhou, J. Hazard. Mater. 166 (2009) 939–944

[19]Hee-Jin Noh, Dong-Seok Seo, Hwan Kim, Jong-Kook Lee, Mater. Lett. 57 (2003) 2425– 2431

[20]G. Ehrhart, B. Capoen, O. Robbe, Ph. Boy, S. Turrell, M. Bouazaoui, Thin Solid Films 496 (2006) 227 – 233

[21]Nae-Lih Wu, Ton-Fon Wu, J. Am. Ceram. Soc. **83** [12] (2000) 3225–27

[22]Martin C. Heine, Lutz Mädler, Rainer Jossen, Sotiris E. Pratsinis, Combustion and Flame 144 (2006) 809–820

[23]Ali Akbar Ashkarran, Seyedeh Arezoo Ahmadi Afshar, Seyed Mahyad Aghigh, Mona kavianipour, Polyhedron 29 (2010) 1370–1374

[24]Jiahe Liang, Zhaoxiang Deng, Xin Jiang, Fuli Li, Yadong Li, Inorg. Chem. 41 (2002) 3602-3604

[25]Cuikun Lin, Cuimiao Zhang, Jun Lin, J. Phys. Chem. C 111(2007) 3300-3307

[26]Jiahe Linang, Xin Jiang, Ge Liu, Zhaoxiang Deng, Jing Zhuang, Fuli Li, Yadong Li, *Mater. Res. Bull.* **38** 38 (2003) 161-168

[27]P.V. Ananthapadmanabhan, T.K. Thiyagarajan, K.P. Sreekumar, N. Venkatramani, Scripta Materialia 50 (2004)

[28]P.V.Ananthapadmanabhan, Patrick R. Taylor, Journal of Alloys and Compounds 287 (1999) 121-125

[29]P.V.Ananthapadmanabhan, Patrick R. Taylor, Wenxian Zhu, Journal of Alloys and Compounds 287 (1999) 126-129
[30]P.V.Ananthapadmanabhan, K.P. Sreekumar, N. Venkatramani, R. Kameswaran, C.C. Dias, S.C. Mishra , Bulletin of Materials Science 19 (3) (1996) 559-564
[31]J.I. Langford, A.J.C. Wilson, J. Appl. Cryst. 11 (1978) 102-113.
[32]A. Feinberg, C.H. Perry, J.Phys. Chem. Solids. 42 (1981) 513-518
[33]Li Shi, Kam-Chung Tin, Ning-Bew Wong, Journal of materials science 34 (1999) 3367 – 3374
[34]Albertina Cabanas, Jawwad A. Darr, Edward Lester, Martyn Poliakoff J.Mater. Chem. 11 (2001) 561-568
[35]Fengxi Chen, Qi Hong, Guo-Qin Xu, T.S.Andy Hor, Shoucang Shen, J.Am.Ceram.Soc., 88[9] (2005) 2649-2651
[36]Weizhen li, Hua Huang, Hongjia Li, Wei Zhang, Haichao Liu, Langmuir 24 (2008) 8353 – 8366
[37]Yanxia Hao, Jiansheng Li, Xujie Yang, Xin Wang, Lude Lu materials Science and Engineering A 367 (2004) 243-247
[38]Shougang Chen, Yansheng Yin, Daoping Wang, Yingcai Liu, Xin Wang Journal of Crystal Growth 282 (2005) 498-505
[39]P.V.Ananthapadmanabhan, M. Vijay, T.K. Thiyagarajan, Plasma Sci. & Technology 12 (4) (2010) 426-432
[40]Michael W. Pitcher, Sergey V. Ushakov, Alexandra Navrotsky, Brain F. Woodfield, Guangshe Li, Juliana Boerio-Goates, Brain M. Tissue, J. Am. Ceram. Soc., 88[1] (2005) 160-167
[41]T. Mitsuhashi, T. Ikegami, A. Watanabe, and S. Matsuda, Proc. Int. Conf.Intell. Mater., 1, 155–8 (1992).
[42]A. Suresh, M. J. Mayo, W. D. Porter, and C. J. Rawn, J Am. Ceram.Soc., 86 [2] 360–2 (2003).
[43]G. S ˇ tefanic´ and S. Music´, Croat. Chem. Acta, 75 [3] 727–67 (2002).

Table 1:
Operating parameters.

Operating parameters	**Values**
Torch input power (KW)	10-16
Arc voltage (V)	40
Arc current (A)	250-400
Primary plasma gas(Ar) flow rate (LPM)	30
Secondary gas($N_{2)}$ flow rate (LPM)	2
Carrier gas (Ar) flow rate (LPM)	10
Reactive gas (O_2) flow rate (LPM)	20
Precursor powder (ZrH_2) feed rate (g/min)	5

Table 2:
Sample identification.

Sample	Region of collection
A	Torch head
B	Reactor
C	Flanges of collection chamber

Table 3:
Phase composition of powder collected from different regions.

Sample	Monoclinic X_m (%)	Tetragonal X_t (%)
A	80	20
B	62	38
C	56	44

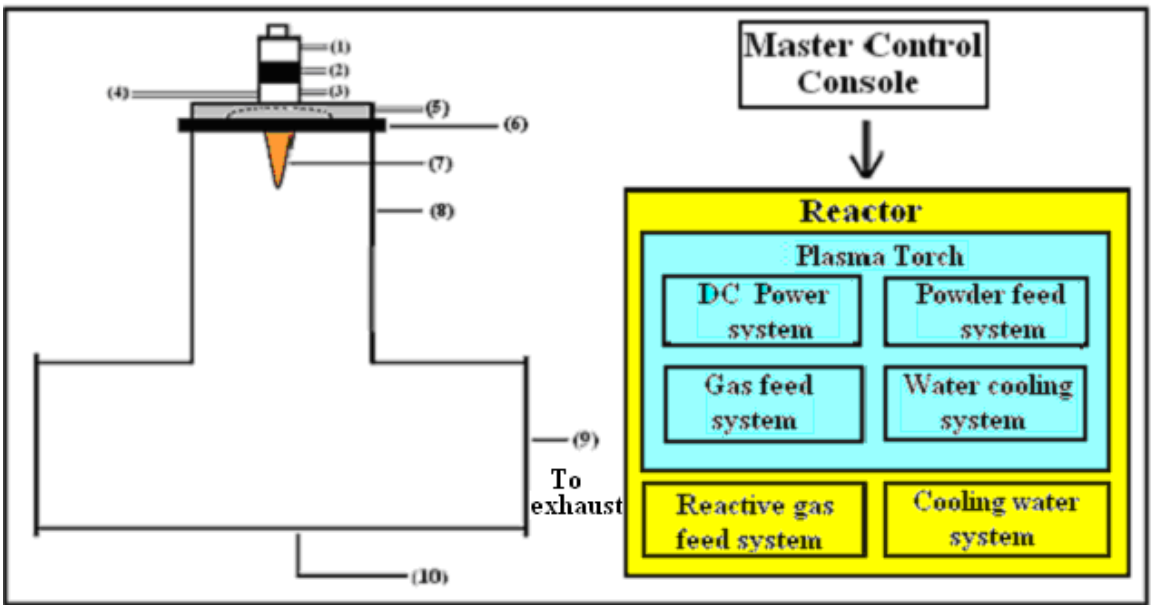

Fig.1 Schematic of plasma reactor (1- water cooled cathode with power cable, 2- insulator module plasma gas feed port, 3 - water cooled anode with power cable, 4 - powder feed port, 5 - reactive gas injecting flange with feed port, 6- torch head section, 7 - plasma jet, 8 - water cooled reactor region, 9 - flange, 10 - collection chamber)

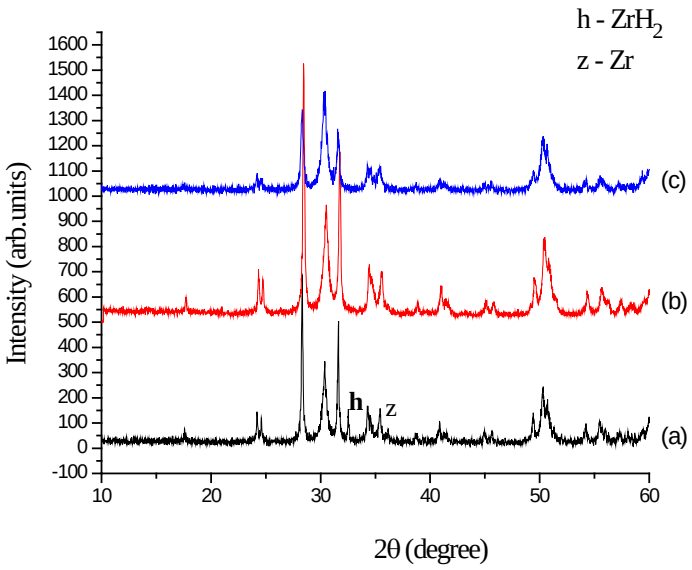

Fig. 2 X-ray diffraction patterns of nano-crystalline ZrO_2 powders synthesized at different powers: (a) 10 kW, (b) 12 kW and (c) 16 kW

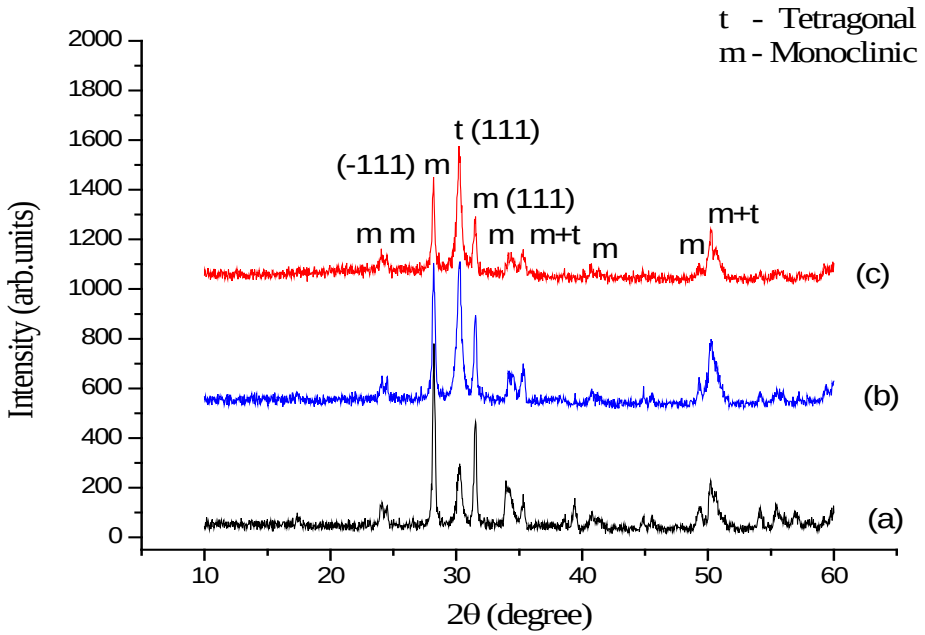

Fig. 3 X-ray diffraction pattern of reactive plasma synthesized nanocrystalline ZrO_2, collected from different locations (16 kW): (a) sample A, (b) sample B and (c) sample C

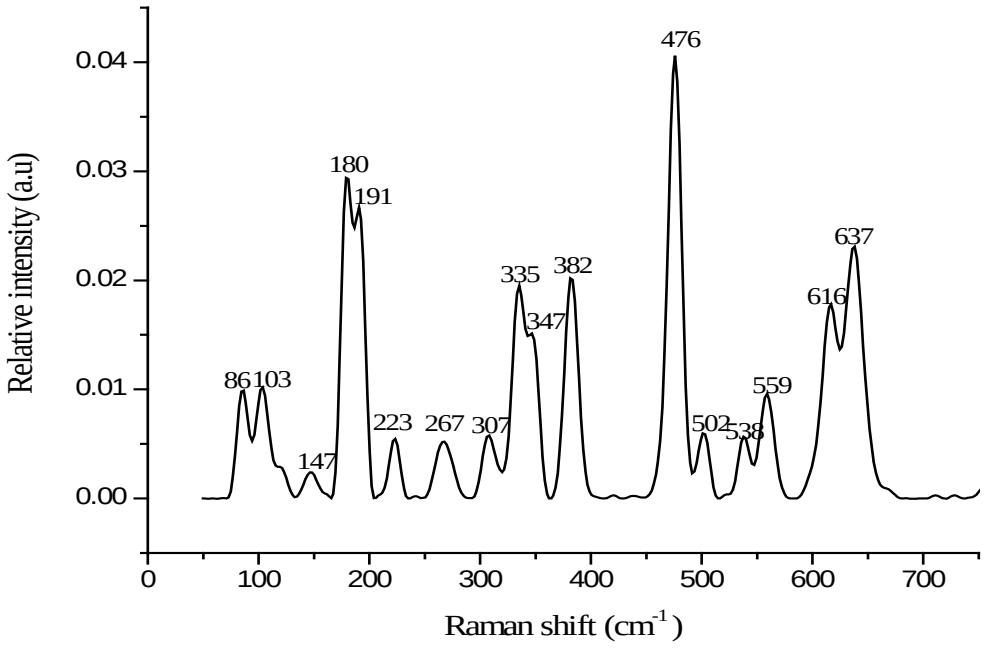

Fig. 4 Raman spectra of reactive plasma synthesized nanocrystalline ZrO_2- sample C

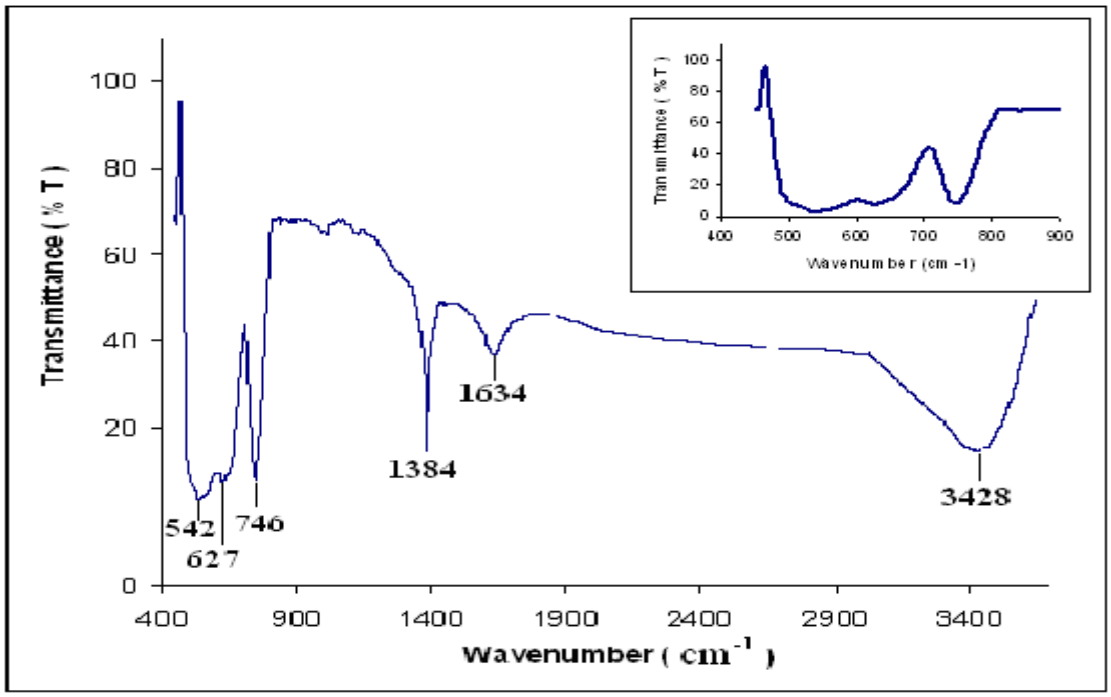

Fig.5 FT-IR spectra of reactive plasma synthesized nanocrystalline ZrO_2- sample C

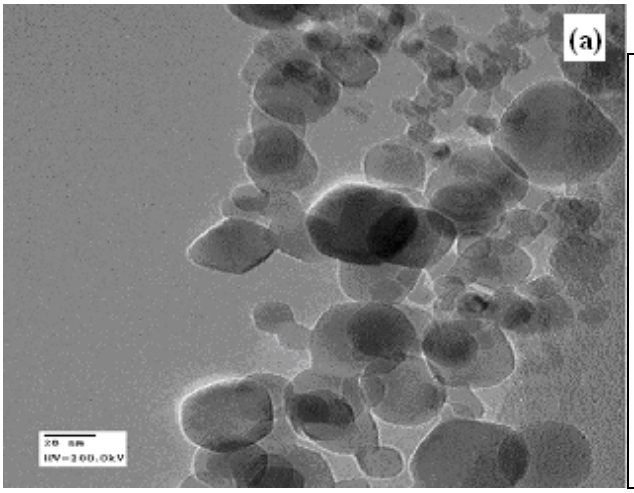
(a)

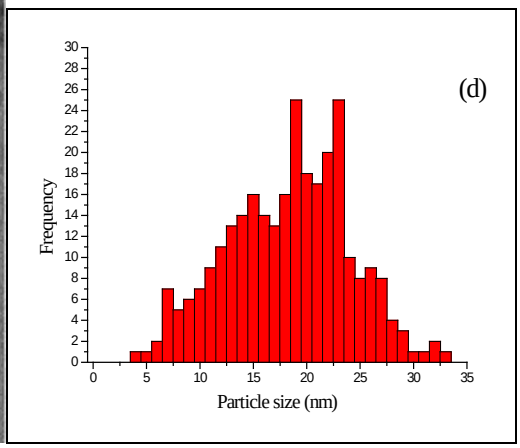
(d)
Frequency
Particle size (nm)
0
2
4
6
8
10
12
14
16
18
20
22
24
26
28
30
0
5
10
15
20
25
30
35

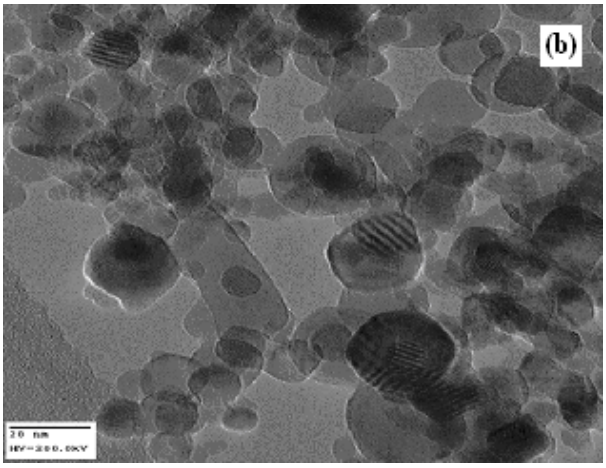
(b)

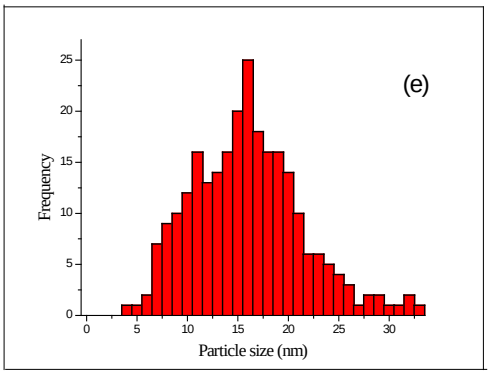
(e)
Frequency
Particle size (nm)
0
5
10
15
20
25
0
5
10
15
20
25
30

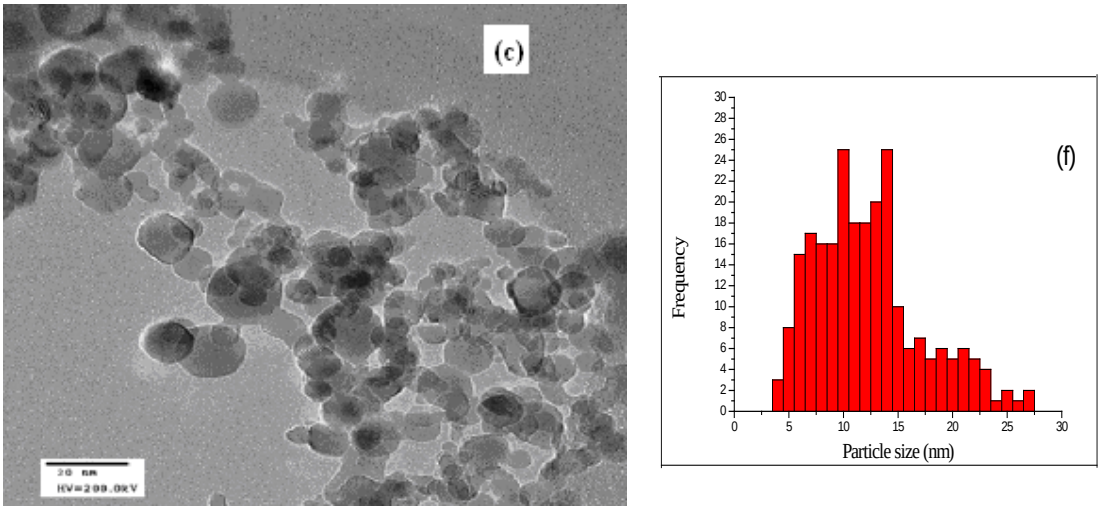

Fig. 6 TEM photographs and particle size distribution of reactive plasma synthesized nanocrystalline ZrO_2: (a) and (d) sample A, (b) and (e) sample B, (c) and (f) sample C